Atmospheric Boundary-Layer and Flutter Computations Using CFD Model of the Transonic Dynamics Tunnel

Pawel Chwalowski, Thomas G. Ivanco, and Jennifer Heeg
Aeroelasticity Branch, NASA Langley Research Center, Hampton, VA 23681
USA

Pawel.Chwalowski@nasa.gov

ABSTRACT

This paper presents two Computational Fluid Dynamics (CFD) models of the flow in the NASA Langley Research Center Transonic Dynamics Tunnel (TDT). The first computational model describes the generation of an atmospheric-boundary-layer (ABL) profile inside the tunnel. An ABL, which includes both a wind profile and turbulence content, is one of the aerodynamic characteristics affecting the occurrence of wind-induced oscillations for a launch vehicle sitting on a pad. The challenging part of this analysis was modeling the turbulent flow inside the tunnel. This is due to the special ABL-generating hardware that was installed at the entrance of the TDT test section in order to change the downstream velocity profile and to introduce velocity fluctuations into the flow. The second CFD model builds on the computational aeroelastic results that were generated in support of the second Aeroelastic Prediction Workshop (AePW) for the NASA Benchmark Supercritical Wing (BSCW) configuration. During the AePW, the wing-only configuration (classical free-air model) was analyzed. In the current study, the flutter computations were conducted on the configuration as it was mounted in the TDT during the experiment. This includes the wing and the splitter plate assembly that was attached to the wind-tunnel walls. The preliminary results show that the wind-tunnel walls marginally affect flutter prediction.

1.0 INTRODUCTION

The Transonic Dynamics Tunnel (TDT), located at the NASA Langley Research Center, is a continuous-flow, closed circuit, variable pressure wind tunnel, with a 16- by 16-foot slotted test section with cropped corners. It has the capability to use either air or R-134a heavy gas as the test medium. In this study, experimental data acquired in either air or the R-134a test medium were compared with the computational data. The TDT's unique capabilities are well described and summarized in the publication by Ivanco [1], where he states the following: "Typically regarded as the world's premier aeroelastic test facility, TDT fulfills a unique niche in the wind tunnel infrastructure as a result of its unparalleled ability to manipulate fluid-structure scaling parameters." A sketch and plan view of the TDT are shown in Figures 1-1a and 1-1b, respectively.

The development of a Computational Fluid Dynamics (CFD) model of the TDT allows for realistic comparisons of the experimental data collected in the tunnel with computational data. By including the tunnel walls in the computational model, for example, the uncertainty associated with the tunnel wall interference effects is significantly reduced. In 2012, an initial benchmarking of the CFD model of the TDT was conducted using experimental data obtained during empty tunnel calibration [2]. The fundamental parameters matched in the validation between the experiments and computations included boundary-layer profiles, wall pressures, and centerline Mach number at various flow conditions.

Since its initial benchmarking, the TDT CFD model has been used to predict a flutter event that occurred during testing of a full-span generic fighter flutter model in the TDT [3,4]. During this experiment, flutter occurred, damaging the wings of the test article. This flutter event was computed, assuming first a free-air model and then a model including the wind-tunnel walls. The assessment from that study was that the wind-tunnel walls marginally affected the response of the aircraft model and that the flutter prediction for both computational models was essentially the same [5].

This paper discusses two additional CFD modeling efforts using the CFD tunnel model. The first numerical study supplemented an experimental test campaign completed in the TDT three years ago. The purpose was to develop representative atmospheric boundary layer (ABL) profiles for three different launch pad sites [6]. An ABL, which includes both an average wind profile and turbulence content, is one of the aerodynamic characteristics affecting the occurrence of wind-induced oscillations of a launch vehicle sitting on a launch pad. The primary purpose was to determine if the CFD software is capable of predicting an ABL profile. The secondary purpose was to demonstrate that tunnel walls might have an effect on the experimental data. With that in mind, the computational models were constructed both with and without tunnel walls to quantify the tunnel-wall effect on the prediction of the ABL.

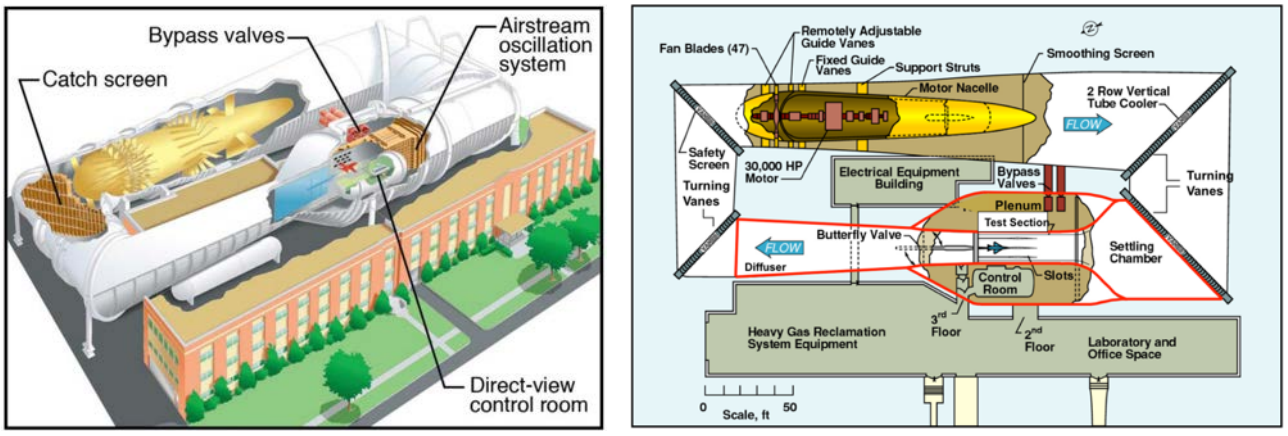

(a) Sketch of the TDT with key features. **(b) TDT plan view with numerical domain marked in red.**

Figure 1-1: TDT description.

The second numerical study supplemented work done for the second AIAA Aeroelastic Prediction Workshop (AePW), which took place in conjunction with the AIAA SciTech 2016 Conference in San Diego, California. For that workshop, the computational aeroelasticity community was challenged to analyze one configuration of the NASA Benchmark Supercritical Wing (BSCW) at three conditions and to present their results at the workshop. The BSCW configuration was first tested in the TDT in 1991, with the wing mounted on the TDT Pitch And Plunge Apparatus (PAPA) to obtain the flutter boundary at various Mach numbers and angles of attack for a two-degree-of-freedom (pitch and plunge) system. In 2000, the wing was tested again, this time on a TDT mounting mechanism called the Oscillating Turntable (OTT). The purpose of the OTT tests was to measure aerodynamic response during sinusoidal (forced) pitch oscillation of the wing. The experimental data indicated that the BSCW exhibited a strong shock and boundary-layer-induced separated flow at a moderate angle of attack at transonic conditions. The computations of the transonic flow, in conjunction with the flutter boundary predictions, were the focus of the workshop [7]. In this study, the flutter boundary computation was repeated at one condition by constructing a computational domain exactly matching the experimental wind-tunnel assembly.

2.0 ABL-PRODUCING HARDWARE USED IN THE TDT

In the TDT ABL experiments, Irwin spires [8] were installed at the entrance to the test section in the region of the converging nozzle. This allowed for an approximate 42-foot distance, called the fetch length, for the flow to develop the desired characteristics and the velocity profile shape to simulate an ABL prior to impacting a launch vehicle model that would be mounted on the TDT's floor turntable. In addition, floor-mounted roughness elements, either 3-inch or 6-inch wooden cubes/blocks, were installed in various configurations along the fetch length to help sustain the spire-induced turbulence and to alter the boundary-layer profile. A photograph of one of the tested spire-and-cube (or roughness elements) configurations is presented in Figure 2-1. The pictures in Figures 2-2a and 2-2b depict an example of the size and location of the spires and cubes. Note that the measurement of the ABL profile in the TDT is at the location denoted as TS 72 in Figure 2-2b. This refers to the TDT reference tunnel station of 72 feet, which is located at the center of the turntable, as shown in Figures 2-2a and 2-2b. This is the mounting location for the launch vehicle associated with this work. While several spire-plus-cube configurations were tested in the TDT, the corresponding CFD study was only done for two configurations: one attempting to match the average ABL at the Cape Canaveral Air Force Station Space Launch Complex 40 (SLC-40) and the other attempting to match the average ABL at the Kennedy Space Center Launch Complex 39a (SLC-39), both in Florida. The difference between the two wind-tunnel ABL configurations is that the SLC-40 configuration included both spires and cubes, while the SLC-39 configuration consisted of spires only. The top view schematic of the SLC-40 spire-and-cube configuration is shown in Figure 2-3. In this paper, only the CFD results from the SLC-40 study are presented. The results from the SLC-39 study can be found in reference [9].

Data for ABL characterization were acquired with an instrumented flow survey rake positioned in the tunnel such that measurements were obtained at approximately TS 72, which corresponded to the center of the floor turntable where the launch vehicle models would be located [6]. The rake is identified in Figure 2-1. Instruments were distributed along the 12-foot span rake in one-foot increments and consisted of four steady pitot-static pressure probes, two unsteady total pressure probes, two unsteady static pressure probes, two unsteady five-hole probes, and a total temperature probe. The unsteady five-hole probes were used to derive time histories of velocity in all three axes.

The instrumented rake was mounted on a traversing and rolling sting. During testing, tunnel conditions were held constant while the rake was traversed vertically and rotated to various angles in order to map the flow volume. The rake was also inverted so that complementary instruments, such as steady versus unsteady pressure probes, could obtain measurements at the same flow position. Measurements were taken in vertical increments of one foot and were obtained as close to the test section ceiling and turntable face as the sting support system would safely allow, approximately eight and six inches, respectively.

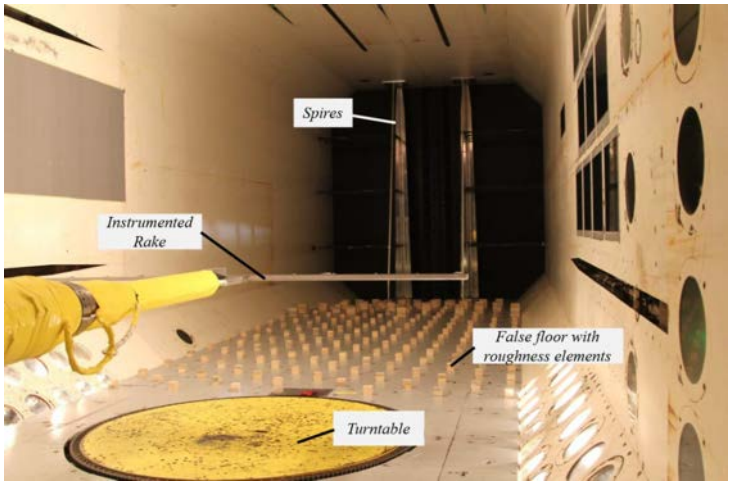

Figure 2-1: Photo of a sample configuration of spire and roughness elements (blocks) installed in the TDT, with instrumentation flow survey rake in the foreground, looking upstream.

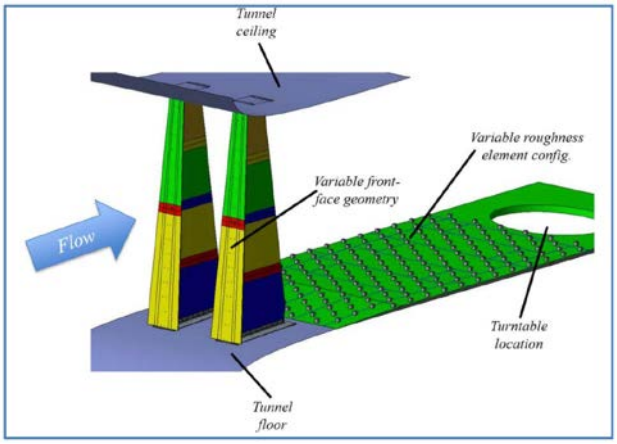

(a) Irwin spire shape and roughness blocks.

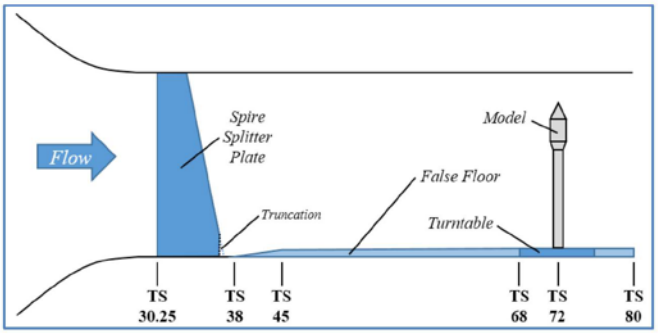

(b) Location of spires in the TDT.

Figure 2-2: Modification to TDT for ABL profile measurement.

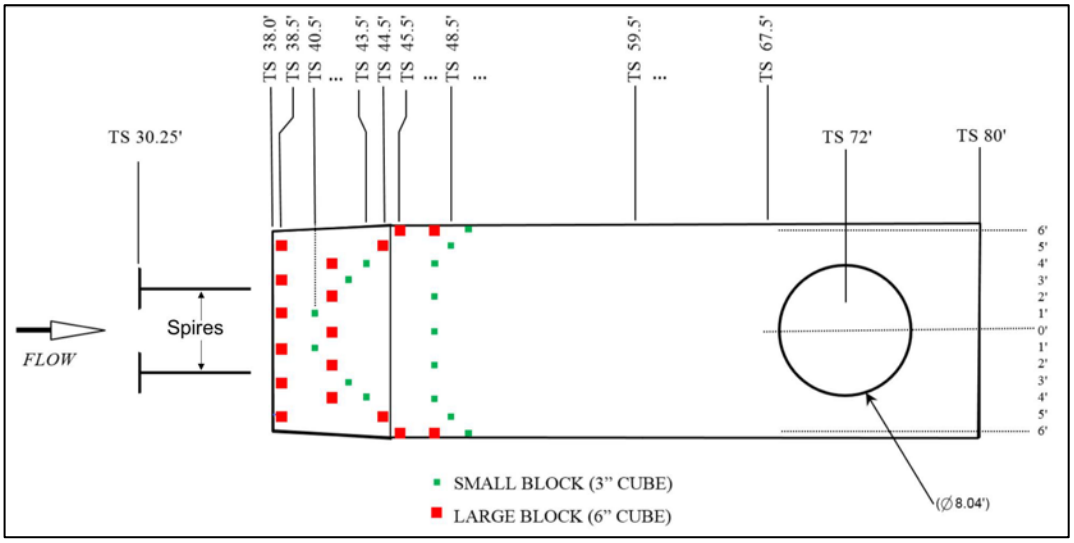

Figure 2-3: Top view of SLC-40 spire locations and roughness block distribution with key features of the test section, tunnel stations in feet.

3.0 COMPUTATIONAL DOMAIN AND MESH

In the TDT plan view shown in Figure 1-1b, the red line around the test section of the tunnel outlines the computational domain used in the CFD analyses. The domain begins with the settling chamber and continues into the test section leg, where it is connected with the plenum via slots in all four walls and a system of reentry flaps. The domain ends at the exit plane of the diffuser. The shape of the computational domain at the settling chamber is not desirable for the numerical analysis because of the corners where the walls of the chamber meet the turning vanes. However, to include the turning vanes in the computational model together with the rest of the tunnel geometry was too computationally expensive. Therefore, the vanes were excluded from the CFD model.

This study utilizes an 'as-built' surface geometry of the TDT as opposed to 'per-drawing', which is the idealized geometry provided in the drawing plans. The same approach was used by Nayani [10] in his analysis of the NASA Langley Research Center 14- by 22-Foot Subsonic Tunnel. To obtain 'as built' geometry for both tunnels, laser scans of the desired regions were conducted. For the TDT test section, the laser scan produced a point cloud database of approximately 15.5 million points through which surfaces were fitted in preparation for grid generation. The details of the surface-fitting process can be found in reference [2].

Unstructured tetrahedral grids were used in this study. They were generated using VGRID [11] with input prepared using GridTool [12]. The tetrahedral elements within the boundary layer were converted into prism elements using preprocessing options within the NASA Langley FUN3D software [13]. The first-cell height away from the wall was set to 9×10^{-6} feet, which ensured the average $y^+ < 1$. For each case considered in this study, (1) empty tunnel and (2) tunnel with spires and blocks, two meshes with consistent size and resolution were used, which for simplicity, are labeled as 'Mesh A' and 'Mesh B' in this paper. Mesh A is considered a coarse mesh, and for the SLC-40 configuration consists of about 89 million nodes. Mesh B for the SLC-40

configuration was constructed in two steps. First, a global refinement was done on Mesh A, which resulted in a 109-million-node mesh. Then, a local refinement was performed between the spires and TS 72 that resulted in a 130-million-node mesh.

Figure 3-1 shows the outside surface mesh of the TDT computational domain using Mesh B. Figure 3-2a depicts the ABL hardware setup inside the TDT test section. Figure 3-2b shows a closeup view of the region and surface mesh inside the tunnel as depicted in Figure 3-2a. Figures 3-2c and 3-2d show the mesh distribution at the TS 72 cross section for Mesh A and Mesh B, respectively. Note that the instrumented rake described earlier was not included in the computational model.

Figure 3-2 also identifies the false floor used during tests when the floor turntable is installed. The false floor serves as an aerodynamic fairing around the turntable and extends from TS 38 to TS 80. Its leading edge is a linear ramp that pushes the floor of the tunnel 5 inches above the permanent floor.

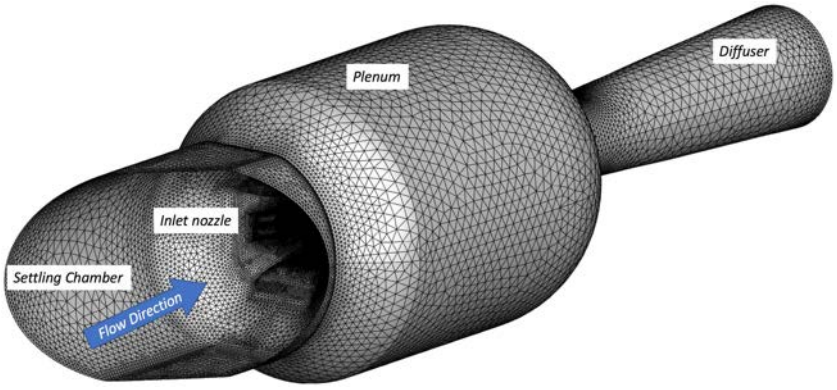

Figure 3-1: TDT computational mesh example; an outside view, Mesh B.

4.0 COMPUTATIONAL APPROACH

4.1 Flow Solver

FUN3D software [13], which was developed at the NASA Langley Research Center, was used in this analysis. FUN3D is a finite-volume, unstructured-grid, node-based, mixed-element Unsteady Reynolds-averaged Navier-Stokes (URANS) flow solver. Various turbulence models are available. The flow condition of interest for this study was Mach 0.25 in air, so the flux limitation was not needed. Inviscid fluxes were computed using the Roe flux-difference splitting scheme [14]. For the asymptotically-steady cases under consideration, time integration was accomplished by an Euler implicit backwards difference scheme, with local time stepping to accelerate convergence. The unsteady results were computed and compared using the Spalart-Allmaras (SA) [15] turbulence model and Modified Delayed Detached Eddy Simulation (MDDES) [16]. The advancement in time for unsteady computations was accomplished using a second-order backward difference scheme [17].

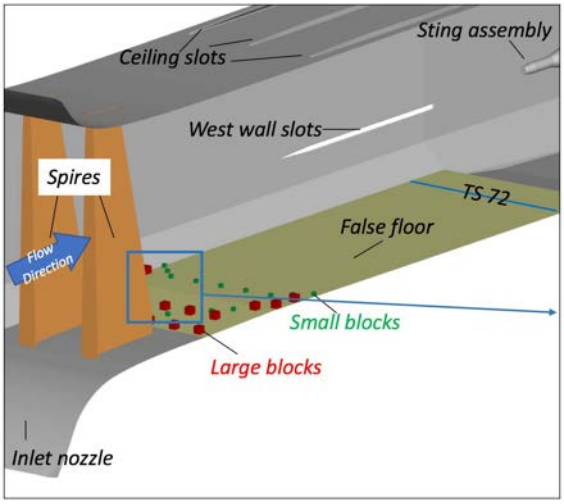

(a) Inside view of the hardware setup in CFD model.

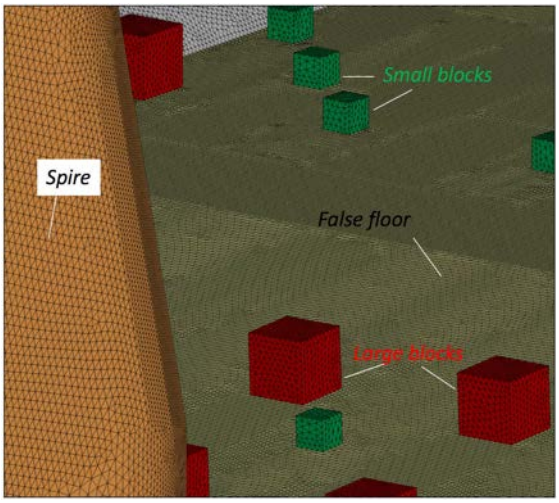

(b) Zoomed-in region with surface mesh.

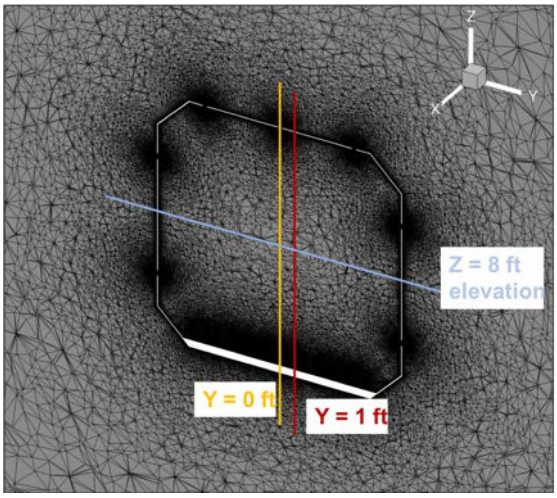

(c) Cross section of Mesh A at TS 72.

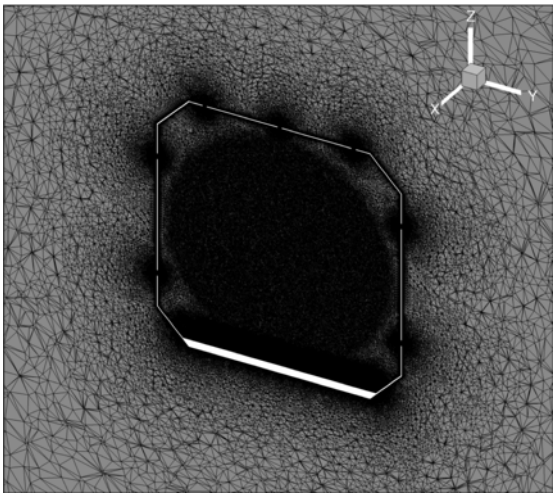

(d) Cross section of Mesh B at TS 72.

Figure 3-2: Hardware setup and computational mesh for the SLC-40 configuration.

4.2 Boundary Conditions

For this study, a total pressure and total temperature boundary condition was used at the settling chamber. The shape of the computational domain at the inlet required specification of the inlet flow angle at the plane where the turning vanes are located (see Figure 1-1b). This angle was measured to be 38°. At the exit of the diffuser, a back pressure boundary condition was used. Back pressure is not a measured quantity in the TDT, so the value was iterated to achieve the desired Mach number in the test section. The desired Mach number is determined based on the computed static pressure in the plenum and the total pressure at the inlet. Every computation was run 'from scratch' whenever the back pressure was changed. This procedure was adopted when it was observed that restarting a solution from the previous solution, after changing the back pressure, resulted in oscillations in the flow field requiring many iterations to damp out.

4.3 Solution Process

The first step in the solution process was to initialize the flow to total pressure and total temperature in the settling chamber and to the static pressure elsewhere in the computational domain. The steady-state solution was then obtained. The steady-state cases in this study were run for about 7,000 iterations to achieve an approximate seven order-of-magnitude drop in residuals. Each steady-state computation using Mesh B took approximately 6 hours on 784 Broadwell cores on the NASA Advanced Supercomputing (NAS) Pleiades supercomputer. The unsteady solutions were always restarted from the steady-state solution.

In a typical unsteady computation, the time-step size is chosen based on the fraction of the time it takes a fluid particle to travel a characteristic distance. For example, in the case of an airplane simulation, a mean aerodynamic chord is usually chosen as a characteristic distance. In this study, we chose frequencies of interest, between 6 Hz and 190 Hz, as a guide to compute the time-step size. Based on the 190 Hz frequency and a 1/200 fraction, the physical time-step size is about 2.6×10^{-5} seconds. This time-step size is labeled here as Time 3. Two additional timestep sizes were also considered: five times (Time 2) and 25 times (Time 1) larger than the Time 3 time-step size. The unsteady computations were first restarted from the steady-state solution using the largest time-step size and the flow solver was run for about 15,000 time steps. Then, the computation was restarted with the intermediate time-step size, and the flow solver was run for another 15,000 time steps. Finally, the smallest time-step size, Time 3, was used to obtain the solution. This process allowed the time-averaged quantities to be obtained from each individual phase of the solution. The computational results with the Time 1 and Time 2 time-step sizes are essentially the same, and therefore, all the results shown in Section 5 below were obtained with the Time 2 time-step size only. The results obtained with Time 3 are considered preliminary, because not enough time-record data were obtained for averaging purposes. The first phase of the unsteady computation using Mesh B and Time 1 took approximately 15 days on 784 Broadwell cores on the Pleiades supercomputer.

5.0 RESULTS

5.1 TDT Model

The ABL consists of two quantities: the boundary-layer profile and the velocity turbulence intensity profile. The computed and experimental boundary-layer profiles presented here are plotted as the mean velocity normalized by the reference velocity as a function of tunnel elevation at the lateral center of the tunnel, Y = 0 feet at TS 72. The reference velocity is the mean velocity at an elevation of eight feet. The velocity turbulence intensity is computed as the standard deviation of velocity as a function of tunnel elevation at a lateral location of Y = 1 feet (location of the unsteady total pressure probe on the rake [6]) and normalized by the local mean velocity.

The computed ABL profiles for the SLC-40 configuration are shown in Figure 5-1. The results include (1) MDDES computations on both Mesh A and Mesh B for the SLC-40 configuration, (2) the MDDES computation assuming an empty tunnel without spires and blocks (as a reference), (3) the URANS-SA computation on Mesh B only, and (4) the experimental data. While it appears in Figure 5-1a that the URANS-SA simulation produces a boundary-layer profile that closely matches the experimental data, further examination of these results is necessary. Figures 5-2 and 5-3 present the normalized mean velocity extended to Y= ± 1 and ± 2 feet lateral locations for the URANS-SA and MDDES solution on Mesh B, respectively. As seen in Figure 5-2a, the URANS-SA solutions are characterized by a definite shift in lateral direction in boundary-layer profiles. This is in contrast with the MDDES solutions, where the boundary-layer profiles, as presented in Figure 5-3a, stay more constant within the Y= ± 2 feet range. This is also visually represented by the corresponding normalized velocity surfaces at TS 72 shown in

Figures 5-2b and 5-3b. The URANS-SA solution produced steady-state 'valleys' downstream of the spires due to lack of velocity fluctuations. The MDDES solution, on the other hand, computed these fluctuations, and the averaged velocity produced a uniform surface. The effects of the tunnel walls on the velocity distribution are also visible in these figures. In addition, the 'dents' in the velocity surfaces on the top and sides represent flow through the tunnel's slots.

In addition, Figure 5-1 demonstrates the importance of proper mesh density in the MDDES simulations. The computations performed on Mesh B produced a much better agreement with both the experimental boundary-layer profile in Figure 5-1a, and the velocity turbulence intensity data in Figure 5-1b, than the computations on the less dense Mesh A. Figure 5-1 also presents the computed boundary-layer profile and the velocity turbulence intensity profile for an empty tunnel. Clearly, and as designed, the inclusion of the spires and blocks changes the velocity profile and turbulence intensity. It should be noted that the turbulence intensity computed using the URANS-SA method is closer to the empty-tunnel MDDES results than it is to the MDDES SLC-40 configuration results. This is because the URANS-SA solution lacks the velocity fluctuations and produces more of a steady-state flow downstream of the spires. Although the empty tunnel results were obtained using only the MDDES method, it is assumed that the URANS-SA should produce similar profiles. Note that the experimental data in an empty tunnel in R-134a were not obtained during this test campaign, so they are not available for comparison.

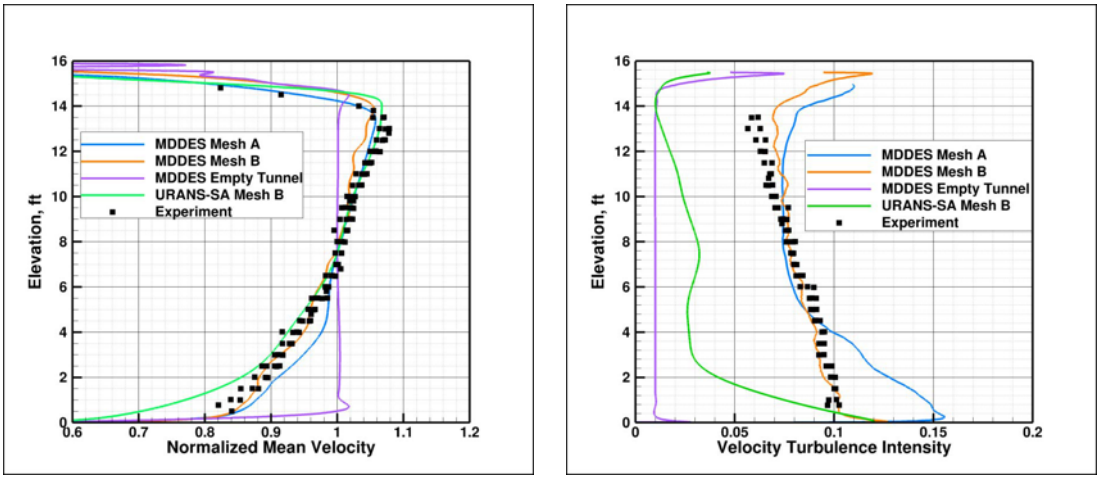

(a) Boundary-layer profile, Y = 0 ft. **(b) Velocity turbulence intensity profile, Y = 1 ft.**

Figure 5-1: Computed SLC-40 ABL profiles: URANS-SA and MDDES solutions, Mesh A and Mesh B, Time 2.

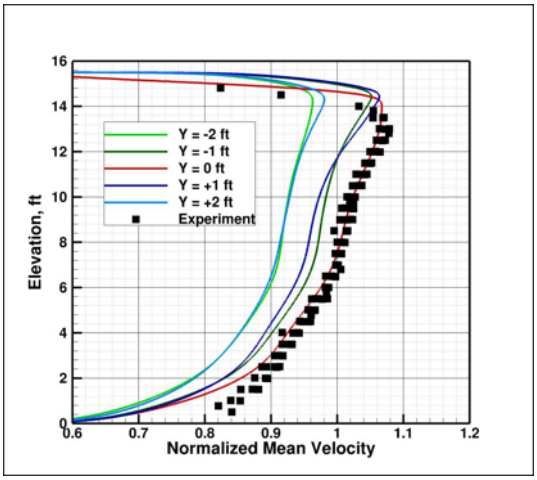

(a) Boundary-layer profile at Y = ±1, ±2, and 0 ft.

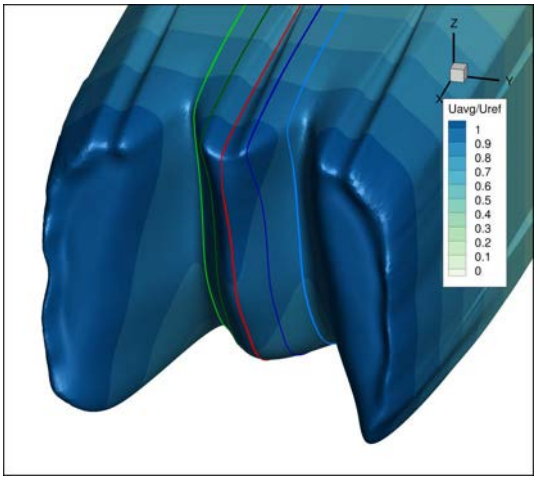

(b) Surface of the normalized mean velocity.

Figure 5-2: Computed (URANS-SA, Mesh B, Time 2) normalized mean velocities near tunnel centerline at TS 72 compared to experimental data at Y = 0 feet, SLC-40.

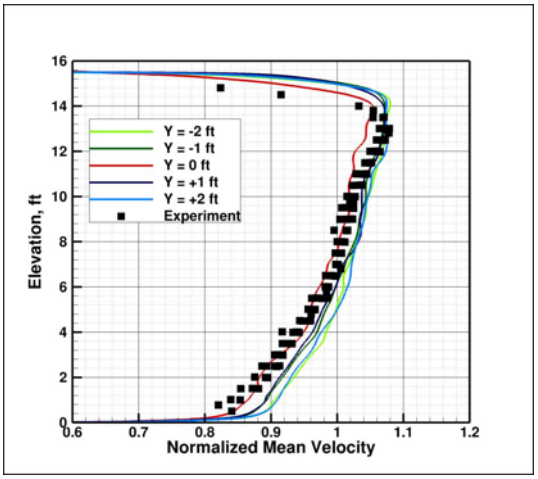

(a) Boundary-layer profile at Y = ±1, ±2, and 0 ft.

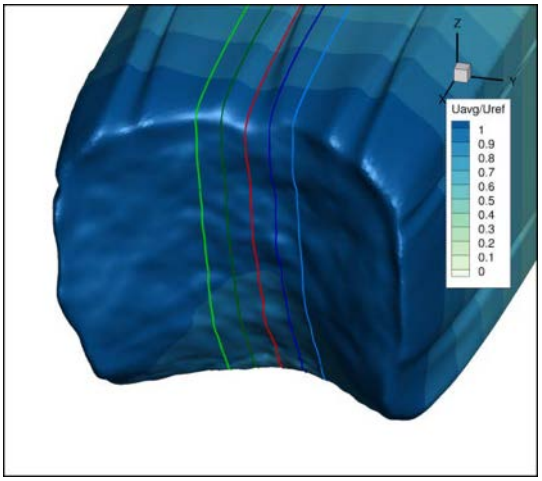

(b) Surface of the normalized mean velocity.

Figure 5-3: Computed (MDDES, Mesh B, Time 2) normalized mean velocities near tunnel centerline at TS 72 compared to experimental data at Y = 0 feet, SLC-40.

The dimensional power spectral density (PSD) at Y = 1 ft and Z = 8 ft (locations identified in Figure 3-2c) computed from the TDT data and the MDDES method is shown in Figure 5-4. The computational turbulence spectra obtained from the MDDES simulations using Mesh B and the three time-step sizes closely match the turbulence spectra from the wind-tunnel in the frequency range up to 90Hz. The spectra were computed using MATLAB®'s 'pwelch' function and a Hamming window with a 50% overlap and a default number of points [18]. The spectra seem to be more dependent on the mesh density (spatial resolution) than the time-step size (temporal

resolution) used in the computations. For example, the solution using Mesh A only matches the experimental data at low frequencies. The turbulence spectra comparison suggests that further mesh refinement is necessary. On the other hand, it appears that the computed ABL profiles (see Figure 5-2) are independent of the high frequency content in turbulence spectra.

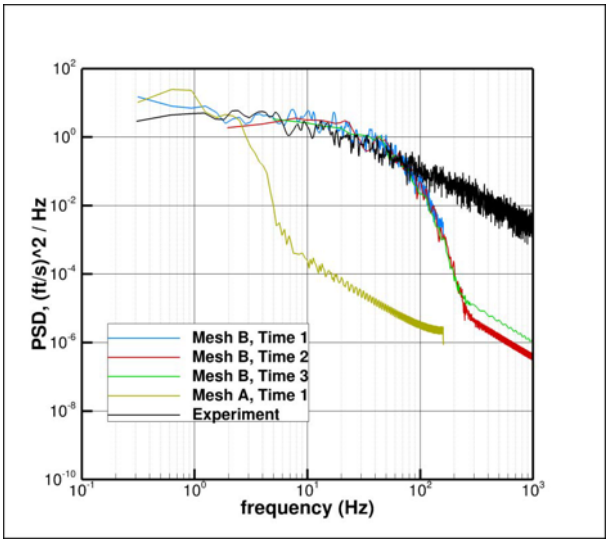

Figure 5-4: Dimensional turbulence spectra computed from measured TDT data at Y = 1 ft and compared with MDDES method using Mesh A and B, and Time 1, Time 2, and Time 3.

5.2 Free-Air Model Versus TDT Model

A computational model of the SLC-40 configuration without the wind-tunnel walls, similar to the one shown in reference [19], was constructed to determine the effect of the walls on the ABL prediction. This model is shown in red in Figure 5-5a. To construct this free-air (FA) model, the wind-tunnel side walls were replaced with planes of symmetry, the wind-tunnel floor was kept as a viscous wall, and the domain was extended vertically. The free-stream boundary condition was applied at the inlet. In addition, the height of the spires was extruded up by about two feet to alleviate potential spire-tip effects on the boundary-layer profile. However, in future analyses, the height of the spires will be increased further per recommendations in reference [6]. The surface roughness block distribution was the same as in the SLC-40 TDT-model configuration. Figure 5-5b shows the MDDES-computed boundary-layer profiles for the FA model, the TDT model using Mesh A, and the experimental data. These results show that the wind-tunnel walls might have a significant effect on the ABL prediction and cannot be ignored in computational models. More analysis is necessary to assess the effects of the computational domain choice on ABL prediction.

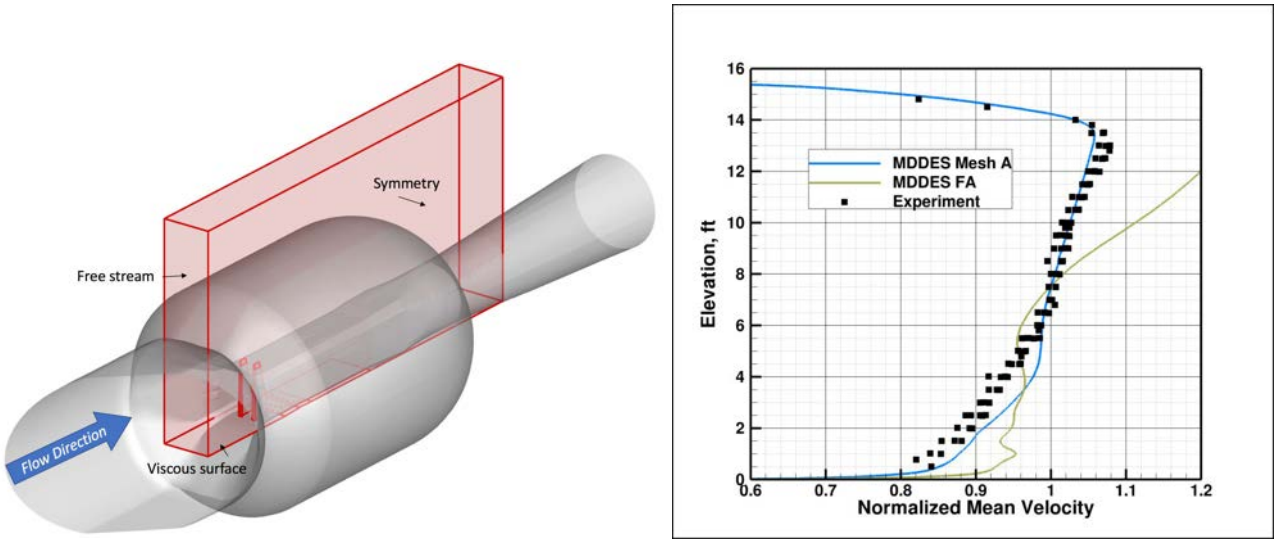

(a) Computational domain. **(b) Boundary-layer profile.**

Figure 5-5: Free-air computational model description and results.

6.0 BENCHMARK SUPERCRITICAL WING FLUTTER COMPUTATIONS

The BSCW model, shown in Figure 6-1, has a simple, rectangular, 16- x 32-inch wing planform, with a NASA SC(2)-0414 airfoil. For both the PAPA and OTT tests discussed in Section 1.0, a large splitter plate, sufficiently offset from the wind-tunnel wall (40 inches), was used to (1) place the wing closer to the tunnel centerline and (2) be outside the tunnel wall boundary layer [20]. The wing was designed to be rigid, with the following structural frequencies for the combined installed wing and OTT mounting system: 24.1 Hz (spanwise first-bending mode), 27.0 Hz (in-plane first-bending mode), and 79.9 Hz (first torsion mode). When installed on the PAPA mount, the combined system frequencies were 3.33 Hz for the plunge mode and 5.20 Hz for the pitch mode. For instrumentation, the model had pressure ports at two chordwise rows at the 60% and 95% span locations, with 22 ports on the upper surface, 17 ports on the lower surface, and 1 port at the leading edge for each row. The BSCW/PAPA data consist of unsteady data at flutter points and averaged data on a rigidified apparatus at the flutter conditions. For this PAPA test, both the inboard row of pressures at the 60% span station and the outboard row at the 95% span station were populated with unsteady in situ pressure transducers. For the OTT test, however, only the inboard row at the 60% span station was populated with unsteady in situ pressure transducers.

For code validations in general, the type of aerodynamic and/or aeroelastic phenomena to be analyzed is important since a validation process typically progresses from simpler to more challenging cases. For the AePW series, the approach being taken is to utilize existing experimental data sets in a building-block approach to incrementally validate targeted aspects of Computational Aeroelasticity (CAE) tools. Each block represents a component of a more complex nonlinear unsteady aeroelastic problem, isolating it such that the contributing physics can be thoroughly investigated. The challenge selected for the first AePW in 2012 was the accurate prediction of unsteady aerodynamic phenomena on essentially rigid, geometrically simple models, with an additional foray into systems with weak coupling between the fluid and the structure. Results from this first workshop helped guide the direction of the second workshop, with analyses extending to include flutter prediction and therefore, increasingly complicated flow fields.

This paper builds on the computational aeroelastic results [21,22] generated for the second AePW, using FUN3D software and BSCW configuration shown in Figure 6-1. While previous publications concentrated on the overall summary of the computational results generated for the workshop for the wing-only configuration including: (1) temporal and spatial resolution, (2) the coupling scheme between the flow and the structural solvers, and (3) the initial excitation conditions, in this paper, we are reporting on the variations of the numerical flutter boundary prediction due to the presence of the tunnel walls. In another words, the computational domain now consists of the exact representation of the wind-tunnel assembly during the experiment. The computational model of the wind-tunnel assembly is shown in Figure 6-2; the computational domain of TDT is based on the description of Figure 3-1. The BSCW is now attached to the PAPA mount. And, the splitter plate is attached to the tunnel walls. The transonic condition considered in these analyses is at Mach 0.74 with 0° angle of attack. The numerical results are compared to the experimental data obtained during the PAPA test in R-12 test medium. Note that Figure 6-2 does not show a diffuser extension in the computational domain. This extension was added to the computational domain to alleviate a potential problem with the reverse flow at the outflow boundary condition. In addition, an automatic numerical wind-tunnel controller [23] was used in the simulations to obtain accurate Mach number in the test section.

The BSCW dynamic analysis was performed in a multistep process. First, the steady CFD solution was obtained

on the rigid body. In the case of a dynamic aeroelastic flutter solution, a static aeroelastic solution was then obtained by restarting the CFD analysis from the rigid-steady solution in a time-accurate mode [24] with a structural modal solver, allowing the grid to deform. A high value of structural damping (0.99) was used so the structure could find its equilibrium position with respect to the mean flow before the dynamic response was started. Finally, the flutter solution was restarted from the static aeroelastic solution by setting the structural damping value to zero and providing an initial excitation ‘kick’ in the form of the generalized velocity. Only URANS-SA computations were performed.

Aeroelastic analysis requires a grid deformation capability. The grid deformation in FUN3D is treated as a linear

elasticity problem. In this approach, the grid points near the body can move significantly, while the points farther

away may not move at all. In addition to the moving body capability, the analysis of the BSCW configuration requires a structural dynamics capability. For a dynamic aeroelastic analysis, FUN3D is capable of being loosely coupled with an external finite element solver [24], or in the case of the linear structural dynamics used in this study, an internal modal structural solver can be utilized [25]. This modal solver is formulated and implemented in FUN3D in a manner similar to other NASA Langley aeroelastic codes (CAP-TSD [26] and CFL3D [27]). For the BSCW computations presented here, the structural modes were obtained via a normal modes analysis (solution 103) with the Finite Element Model (FEM) solver MSC Nastran™ [28]. The modes were then interpolated to the surface mesh using the method developed by Samareh [29]. The BSCW FEM was built by Heeg and is described in reference [21].

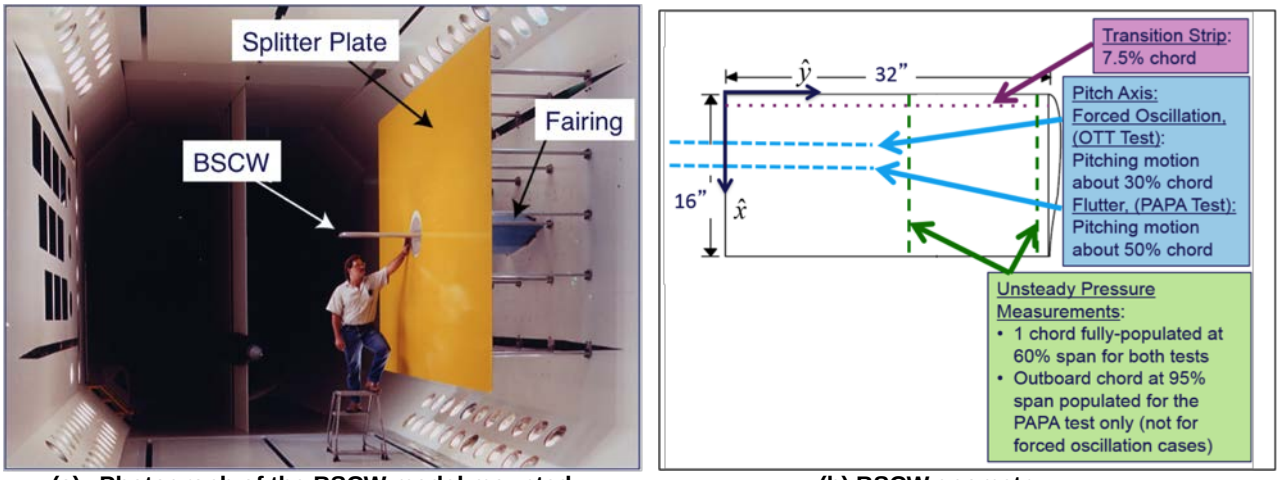

(a) Photograph of the BSCW model mounted on the OTT in the TDT.

(b) BSCW geometry.

Figure 6-1. BSCW model.

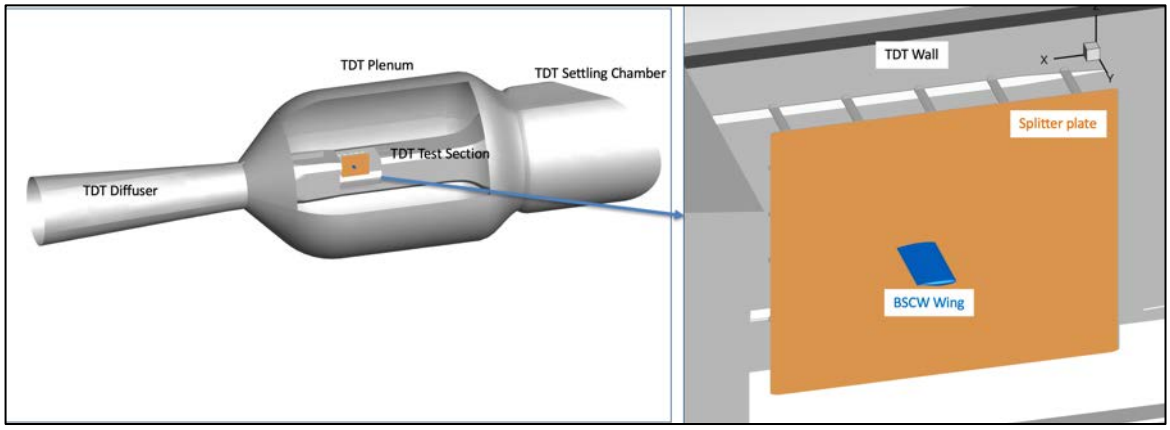

Figure 6-2. Computational model of the BSCW as mounted in the TDT.

As described in the previous section, the second AePW test case involved BSCW flutter prediction on the PAPA mount system at Mach 0.74 and 0° angle of attack. In the analysis, the rigid steady solution was obtained first, followed by the static aeroelastic solution. The third step involved performing several dynamic aeroelastic FUN3D computations with different values of the dynamic pressure in the vicinity of the experimental flutter dynamic pressure. The wing response in the form of the time-varying pitch angle was then computed and used to calculate the damping ratio using a logarithmic decrement method. For a stable solution, the damping ratio is greater than zero, and for an unstable solution, the damping ratio is less than zero. The damping ratio and the dynamic pressure were interpolated, and at zero damping ratio, the dynamic pressure was considered to be the flutter dynamic pressure. Once this flutter dynamic pressure was identified, the corresponding flutter frequency was determined via an interpolation of the frequencies. For this analysis process, dynamic solutions were obtained for the wing-only medium grid at several dynamic pressures, ranging from 1 to 169 psf. The high end of this range, at 169 psf, was chosen because it is the experimentally-obtained flutter dynamic pressure. The resulting computed damping

and frequencies are presented in Figures 6-3a and 6-3b, respectively. An averaged dynamic pressure of 151.7 psf was declared to be the computationally-obtained flutter dynamic pressure for the wing-only configuration, a value that is approximately 10% below the experimental flutter dynamic pressure. The numerical flutter frequency for all three grids was determined to be approximately 4.2 Hz. Similarly, the dynamic pressure of 147 psf was computed to be the flutter dynamic pressure for the wing-inside-the-TDT configuration, a value that is 15% below the experimental flutter dynamic pressure. These results are shown as purple circles in Figures 6-3a and 6-3b. Note, that these flutter computations were obtained using the URANS-SA method, however, based on the ABL computational results, the BSCW flutter prediction needs to be repeated using higher-fidelity methods.

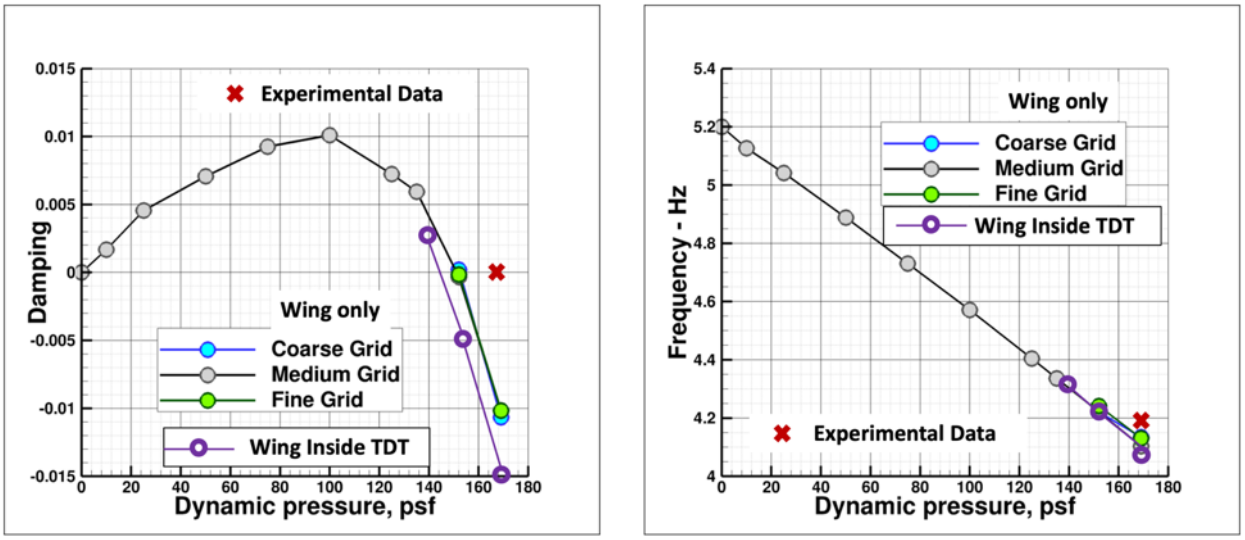

(a) Damping value as a function of dynamic pressure. **(b) Frequency as a function of dynamic pressure.**

Figure 6-3: Search for flutter dynamic pressure and flutter frequency, BSCW model on PAPA mount, Mach 0.74, Re_c = 4.45 × 106, α = 0°, URANS-SA.

7.0 CONCLUDING REMARKS

The first objective of this study was to compute two ABL profiles using the computational model of the TDT. These profiles were computed using both URANS-SA and MDDES solutions and were compared against the experimental data. The results demonstrated that the MDDES solution, using a higher density mesh, produced very good agreement with the experimental data for both the boundary-layer profile and the velocity turbulence intensity profile. The second objective was to compare the computational results obtained in the TDT model with those obtained in a classical free-air model. The results showed that the wind-tunnel walls cannot be ignored in the computational model. Future analysis will extend this work to examine temporal and spatial convergence and the necessary time-record length for velocity averaging.

Follow-up flutter prediction analyses were performed as part of AePW using the NASA Langley FUN3D software. The analyses included identifying the effects of the wind-tunnel walls on flutter prediction. The computationally-obtained flutter dynamic pressure was 10% and 15% below the experimental flutter point for the wing-only and the wing-inside-the-TDT models, respectively, at Mach 0.74 and 0° angle of attack. In general, the flutter onset

prediction moves the result away from the experimental data, rather than toward it. And these results indicate that the presence of the splitter plate and/or tunnel walls reduce the flutter onset condition. However, these analyses were conducted using URANS-SA only. Based on conclusions from the ABL computations, the flutter boundary using the MDDES method needs to be computed. In addition, the flutter analyses were conducted assuming zero structural damping. The exact value of structural damping is not known, but adding small amount of structural damping would move the predictions toward the experimental data. This will be addressed in future studies.

8.0 ACKNOWLEDGMENTS

The computational analyses were conducted at the NASA Advanced Supercomputing Center located at the NASA Ames Research Center. The authors would like to acknowledge help from several members of the Aeroelasticity Branch at the NASA Langley Research Center: Dr. Kevin Jacobson and Ms. Jennifer Pinkerton. In addition, the authors would like to acknowledge discussions with and help from Dr. Christopher Rumsey and Dr. Jan-Renee Carlson from the Computational Aerosciences Branch at the NASA Langley Research Center.

9.0 REFERENCES

[1] Ivanco, T. G. (2013). Unique Testing Capabilities of the NASA Langley Transonic Dynamics Tunnel, an Exercise in Aeroelastic Scaling. AIAA Paper 2013-2625.

[2] Chwalowski, P., Quon, E., and Brynildsen, S. E. (2016). Computational Analysis of the Transonic Dynamics Tunnel. AIAA Paper 2016-1775.

[3] Silva, W. A., Ringertz, U., Stenfelt, G., et al. (2016). Status of the KTH-NASA Wind-Tunnel Test for Acquisition of Transonic Nonlinear Aeroelastic Data. AIAA Paper 2016-2050.

[4] Silva, W. A., Chwalowski, P., Wieseman, C. D., et al. (2017). Computational Results for the KTH-NASA Wind-Tunnel Model Used for Acquisition of Transonic Nonlinear Aeroelastic Data. AIAA Paper 2017-1814.

[5] Chwalowski, P., Silva,W. A.,Wieseman, C. D., et al. (2018). CFD Model of the Transonic Dynamics Tunnel with Applications. NATO AVT-284, May, 2018.

[6] Ivanco, T. G., Keller, D. F., Pinkerton, J. L., et al. (2018). Development of an Atmospheric-Boundary-Layer Profile at the NASA Langley Transonic Dynamics Tunnel. AIAA Paper 2018-5184.

[7] Heeg, J., Chwalowski, P., Schuster, D. M., Raveh, D., Jirasek, A., and Dalenbring, M., (2015). Plans and Example Results for the 2nd AIAA Aeroelastic Prediction Workshop, AIAA Paper 2015-0437, Jan. 2015.

[8] Irwin, H. P. A. H. (1981). The Design of Spires for Wind Simulation. Journal of Wind Engineering and Industrial Aerodynamics. Elsevier, Vol.7, 1981, pp 362-366.

[9] Chwalowski, P. and Ivanco, T. G., (2019). Modeling of an Atmospheric-Boundary-Layer Profile in Support of Experiments in the NASA Langley Transonic Dynamics Tunnel. IFASD-2019-027.

[10] Nayani, S. N., Sellers, W. L., Brynildsen, S. E., et al. (2015). Numerical Study of the High-Speed Leg of a Wind Tunnel. AIAA Paper 2015-2022.

[11] Pirzadeh, S. Z. (2008). Advanced Unstructured Grid Generation for Complex Aerodynamic Applications. AIAA Paper 2008-7178.

[12] Samareh, J. A. (1993). Unstructured Grids on NURBS Surfaces. AIAA Paper 1993-3454.

[13] NASA LaRC, Hampton, VA (2017). FUN3D Manual, v13.2. http://fun3d.larc.nasa.gov.

[14] Roe, P. L. (1981) Approximate Riemann Solvers, Parameter Vectors, and Difference Schemes. Journal of Computational Physics. Vol. 43, No. 2, 1981.

[15] Spalart, P. R. and Allmaras, S. R. (1994). A One-Equation Turbulence Model for Aerodynamic Flows. La Recherche Aerospatiale, No. 1, 1994, pp 5–21.

[16] Vatsa, V. N. and Lockard, D. P. (2010). Assessment of Hybrid RANS/LES Turbulence Models for Aeroacoustics Applications. AIAA Paper 2010-4001.

[17] Vatsa, V. N., Carpenter, M. H., and Lockard, D. P. (2010). Re-evaluation of an Optimized Second Order Backward Difference (BDF2OPT) Scheme for Unsteady Flow Applications, AIAA Paper 2010-122.

[18] http://www.mathworks.com/products/matlab/. The MathWorks, Inc. Natick, Massachusetts, USA.

[19] Hobson-Dupont, M. (2015). The Development of a Small Scale Wind Tunnel Simulating the Atmospheric Boundary Layer. Master's Theses, San Jose State University, Spring 2015.

[20] Schuster, D. M., (2001) Aerodynamic Measurements on a Large Splitter Plate for the NASA Langley Transonic Dynamics Tunnel, NASA TM 2001-210828, March 2001.

[21] Chwalowski, P. and Heeg, J., (2016) FUN3D Analyses in Support of the Second Aeroelastic Prediction Workshop, AIAA Paper 2016-3122, June 2016.

[22] Chwalowski, P. and Heeg, J., Biedron, R. T. (2017). Numerical Investigations of the Benchmark Supercritical Wing in Transonic Flow. AIAA Paper 2017-0190, Jan. 2017.

[23] Carlson, Jan-Renee, (2018). Automated Boundary Conditions for Wind Tunnel Simulations, NASA TM 2018-219812, March 2018.

[24] Biedron, R. T. and Lee-Rausch, E. M., (2008). Rotor Airloads Prediction Using Unstructured Meshes and Loose CFD/CSD Coupling, AIAA Paper 2008-7341, June 2008.

[25] Biedron, R. T. and Thomas, J. L., (2009). Recent Enhancements to the FUN3D Flow Solver for Moving-Mesh Applications, AIAA Paper 2009-1360, Jan. 2009.

[26] Batina, J. T., Seidel, D. A., Bland, S. R., and Bennett, R. M., (1987). Unsteady Transonic Flow Calculations for Realistic Aircraft Configurations, AIAA Paper 1987-0850, Jan. 1987.

[27] Bartels, R. E., Rumsey, C. L., and Biedron, R. T., (2006). CFL3D Version 6.4 - General Usage and Aeroelastic Analysis, NASA TM 2006-214301, March 2006.

[28] MSC Software, MSC Nastran, 2008, http://www.mscsoftware.com/products/msc_nastran.cfm.

[29] Samareh, J. A., (2007). Discrete Data Transfer Technique for Fluid-Structure Interaction, AIAA Paper 2007–4309, June 2007.